# A “Phase Scrambling” Algorithm for Parallel Multislice Simulation of Multiple Phonon and Plasmon Scattering Configurations

B G Mendis

*Microscopy and Microanalysis*, 2023, **29**, 1111–1123
https://doi.org/10.1093/micmic/ozad052
Advance access publication 17 May 2023
**Original Article**

Microscopy AND Microanalysis

# A "Phase Scrambling" Algorithm for Parallel Multislice Simulation of Multiple Phonon and Plasmon Scattering Configurations

**B. G. Mendis**

*Department of Physics, Durham University, South Road, Durham DH1 3LE, UK*
**Corresponding author:** Email: b.g.mendis@durham.ac.uk

## Abstract

Multislice simulations of 4D scanning transmission electron microscopy (4D STEM) data are computationally demanding due to the large number of STEM probe positions that must be calculated. For accurate analysis, inelastic scattering from phonons and plasmons must also be included. However, current frozen phonon and Monte Carlo plasmon techniques require a separate calculation for each different phonon/plasmon configuration, and are therefore not suitable for scaling up to 4D STEM. Here a phase scrambling algorithm (PSA) is proposed, which treats all phonon/plasmon configurations simultaneously. A random phase is introduced to maintain incoherence between the different inelastic scattering events; this is the phase scrambling part of the algorithm. While for most applications, a few tens of frozen phonon iterations are sufficient for convergence, in the case of plasmon scattering as many as tens of thousands of iterations may be required. A PSA is statistically more representative of inelastic scattering, and achieves significant savings in computation time for plasmons. The increase in speed is a pre-requisite for 4D STEM inelastic scattering simulations.

**Key words:** 4D STEM, frozen phonons, multislice simulations, plasmons

## Introduction

The convergent beam electron diffraction (CBED) pattern in a scanning transmission electron microscope (STEM) contains much useful information about the sample. Early applications of CBED include analyzing the space group of crystals (Buxton et al., 1976) and high-angle annular dark-field (HAADF) images with atomic number contrast (Pennycook & Jesson, 1991). In HAADF, the STEM probe is rastered over a specimen area of interest and, for a given probe position, the electron intensity scattered out to high angles is measured by an annular detector. The recent introduction of direct electron detectors has enabled recording the entire CBED pattern at each scan position, a technique known as 4D STEM, due to the fact that two spatial and two reciprocal space coordinates, i.e. ($x$, $y$, $k_x$, $k_y$), are required to index the data. With 4D STEM, several new analyses are possible, such as orientation and strain mapping, differential phase contrast, ptychography, and virtual aperture imaging using electrons scattered to arbitrary angles (for a review see Ophus, 2019). The multislice technique (Cowley & Moodie, 1957, Kirkland, 2010) is the method of choice for simulating most 4D STEM data, although it can be time consuming for large datasets acquired from thick specimens, since a separate multislice simulation must be performed at each scan position. Ophus (2017) has nevertheless introduced a method, called "PRISM", which uses Fourier interpolation to reduce the number of partial plane waves sampled within the STEM probe. PRISM simulations trade some accuracy for an increase in speed, although the loss in accuracy does not significantly affect most routine 4D STEM measurements.

For accurate multislice simulations, however, it is also necessary to include inelastic scattering, especially phonons and plasmons. For example, the role of phonons and thermal diffuse scattering (TDS) has long been recognized in Kikuchi band formation (Kirkland, 2010), as well as HAADF (Pennycook & Jesson, 1991) and annular bright-field images (Findlay et al., 2010). Phonons can be included in multislice simulations using the frozen phonon method of Loane et al. (1991), which assumes that the high energy incident electron passes through the thin specimen so swiftly that the vibrating atoms are effectively "frozen" in their instantaneous positions. By performing multislice simulations on supercells with different frozen phonon configurations and incoherently summing the results, a statistically accurate CBED pattern can be calculated. Although more rigorous quantum mechanical models of phonon excitation have been proposed (e.g., Martin et al., 2009, Forbes et al., 2010), the frozen phonon method can nevertheless be shown to be valid under specific conditions, such as high energy electron beams and thin specimens (Wang, 1998, Van Dyck, 2009). There is a significant computational cost for frozen phonon simulations, since the projected potential for a given slice within the specimen must be re-calculated for every phonon configuration, and typically ten or more configurations are required for reasonable convergence. Peters (2021) introduced a "mixed static potential" (MSP) approach to increase the speed of frozen phonon calculations, which is similar to a concept first proposed by Loane et al. (1991; see equation (8) of their paper). Here the projected potential for only a few frozen phonon configurations are calculated. Assuming uncorrelated atomic

**Received:** January 14, 2023. **Revised:** March 5, 2023. **Accepted:** April 16, 2023

motion, the projected potential for a given slice can be chosen at random from the pre-calculated structures to generate new phonon configurations. Since there are fewer projected potentials to calculate, a significant saving in simulation time is possible, especially for thicker specimens.

Monte Carlo techniques have also been developed to model plasmon scattering within a multislice framework (Mendis, 2019). Here the electron is treated as a point particle, and the plasmon scattering length and scattering angle estimated using computer-generated random numbers, such that the theoretical scattering distributions are statistically reproduced. The use of particle-based Monte Carlo methods in a wave optical, multislice simulation can be theoretically justified for delocalized excitations, such as plasmons (Mendis, 2020). In fact, Monte Carlo plasmon multislice has had success reproducing the angular scattering distribution of high energy electrons (Barthel et al., 2020), as well as identifying the contrast mechanism in electron backscattered diffraction patterns (Mendis et al., 2020). The computational cost is however considerable, with tens of thousands of iterations required for convergence (Barthel et al., 2020, Mendis, 2022*a*). Beyer et al. (2020) have proposed a transition potential for plasmon excitation, which is a somewhat similar concept to the optical potential method for phonon scattering (Hirsch et al., 1965). The transition potential is computationally efficient, and can reproduce the salient features observed in experiment (Beyer et al., 2020).

Inelastic scattering is non-negligible even for specimens as thin as several tens of nanometers. It is therefore desirable to include phonon and plasmon scattering in multislice calculations, although to be useful for 4D STEM, the simulation time must be significantly reduced. A shortcoming of the frozen phonon and Monte Carlo plasmon method is that the different configurations are sampled serially, i.e. a separate calculation must be performed for each phonon or plasmon configuration. In the case of plasmons, this can be extremely wasteful, since many plasmon excitations are low-angle scattering events, and therefore, a large number of iterations are required before the less probable "high"-angle plasmon scattering events are accurately simulated. In this paper, a "phase scrambling" algorithm that models all configurations simultaneously is proposed, thereby improving the speed and, in principle, accuracy of the multislice simulations. The phase scrambling randomizes the phase of the electron wavefunction for the different inelastic scattering paths, thereby preserving incoherence in inelastic scattering. In the following sections, the rationale behind the phase scrambling algorithm (PSA) is presented, along with example simulations from phonon and plasmon scattering.

## Materials and Methods

### Phase Scrambling Algorithm

The principle of the PSA will first be described pedagogically using a highly simplified system, before moving onto the more general case. In the multislice simulation method, the specimen is divided into a series of thin slices along the thickness direction, and the electron wavefunction within each slice is solved sequentially, i.e.

$$\Psi_n(\mathbf{R}) = [\Psi_{n-1}(\mathbf{R})Q_n(\mathbf{R})] \otimes P_n(\mathbf{R}) \quad (1)$$

where $\Psi_n(\mathbf{R})$, $Q_n(\mathbf{R})$ and $P_n(\mathbf{R})$ are the electron wavefunction, phase grating function, and propagation function for a given slice, respectively. The subscript $n$ represents the slice index and $\mathbf{R}$ is the two-dimensional position vector in the plane of the slice. Expressions for $Q_n(\mathbf{R})$ and $P_n(\mathbf{R})$ can be found in Kirkland (2010). Since the incident electron wavefunction $\Psi_0(\mathbf{R})$ is easily calculated from the illumination conditions of the microscope, equation (1) can be solved for successive slices until the specimen exit surface is reached. In practice, Fourier transforms are used to simplify the convolution operation $\otimes$ in equation (1) to a more straightforward multiplication, but this detail is not important for the present discussion.

We shall now describe how PSA can be applied to phonons. Consider a hypothetical system consisting of only two slices "A" and "B", which are crystallographically distinct. Furthermore, assume that each slice has only two phonon configurations. Therefore, slice "A" can have only two unique phase grating functions, which are denoted $Q_{A1}(\mathbf{R})$ and $Q_{A2}(\mathbf{R})$, respectively, and similarly for slice "B". The following expression for the electron wavefunction $\Psi_1(\mathbf{R})$ within slice "A" can be constructed:

$$\Psi_1(\mathbf{R}) = [\Psi_0(\mathbf{R})Q_{A1}(\mathbf{R}) + \Psi_0(\mathbf{R})Q_{A2}(\mathbf{R})] \otimes P_1(\mathbf{R}) \quad (2)$$

Equation (2) is a coherent superposition of the two possible phonon scattering pathways for slice "A". It should be emphasized that equation (2) is a purely mathematical construct and does not have any physical significance. A similar electron wavefunction $\Psi_2(\mathbf{R})$ can be constructed for slice "B':

$$\begin{aligned}\Psi_2(\mathbf{R}) &= [\Psi_1(\mathbf{R})Q_{B1}(\mathbf{R}) + \Psi_1(\mathbf{R})Q_{B2}(\mathbf{R})] \otimes P_2(\mathbf{R}) \\ &= \sum_{i=1}^{2}\sum_{j=1}^{2}[\Psi_0(\mathbf{R})Q_{Ai}(\mathbf{R}) \otimes P_1(\mathbf{R})]Q_{Bj}(\mathbf{R}) \otimes P_2(\mathbf{R}) \\ &= \sum_{i=1}^{2}\sum_{j=1}^{2}\phi_{ij}(\mathbf{R})\end{aligned} \quad (3)$$

The exit wavefunction $\Psi_2(\mathbf{R})$ consists of all the four unique phonon scattering pathways for the system. Note that equation (3) is not normalized, an important observation that will be discussed in more detail later. The CBED intensity $I(\mathbf{k})$ is the square modulus of the Fourier transform for $\Psi_2(\mathbf{R})$:

$$I(\mathbf{k}) = \sum_{i=1}^{2}\sum_{j=1}^{2}|\tilde{\phi}_{ij}(\mathbf{k})|^2 + \text{cross} - \text{terms} \quad (4)$$

where $\tilde{\phi}_{ij}(\mathbf{k})$ is the Fourier transform of $\phi_{ij}(\mathbf{R})$ and $\mathbf{k}$ is a two-dimensional reciprocal space vector. The double summation is the incoherent contribution from the different scattering pathways, and is the term measured experimentally. The $I(\mathbf{k})$ in equation (4) is inaccurate due to the cross-terms resulting from interference between different $\tilde{\phi}_{ij}(\mathbf{k})$. This error is because the individual scattering pathways were treated coherently in equations (2) and (3). To break this coherence, we introduce a random phase shift for each of the scattering events. This is the principle behind "phase scrambling" and PSA. For example, equation (2) is modified to:

$$\Psi_1(\mathbf{R}) = [e^{i\theta_1}\Psi_0(\mathbf{R})Q_{A1}(\mathbf{R}) + e^{i\theta_2}\Psi_0(\mathbf{R})Q_{A2}(\mathbf{R})] \otimes P_1(\mathbf{R}) \quad (5)$$

where the phase angles $\theta_1$ and $\theta_2$ are chosen at random using a random number generator in the computer (strictly speaking, since the phase is arbitrarily defined, we can set $\theta_1$ to

zero and chose a random non-zero phase for only $\theta_2$). Since $\theta_1$ and $\theta_2$ are selected at random, there is no well-defined phase relationship between two phonon scattering events in equation (5). A similar modification is made to $\Psi_2(\mathbf{R})$ in equation (3), i.e.

$$\Psi_2(\mathbf{R}) = [e^{i\theta_3}\Psi_1(\mathbf{R})Q_{B1}(\mathbf{R}) + e^{i\theta_4}\Psi_1(\mathbf{R})Q_{B2}(\mathbf{R})] \otimes P_2(\mathbf{R}) \quad (6)$$

where $\Psi_1(\mathbf{R})$ is the wavefunction in equation (5), and $\theta_3$, $\theta_4$ are two new random phase angles. Multiple electron wavefunctions can be generated by simply changing the phase angles at random in a given PSA iteration. The phase angles are retained in the cross-terms of equation (4), but not in the double summation. Therefore, by summing $I(\mathbf{k})$ for several PSA iterations, the cross-terms should eventually become negligible due to the phase angles being random, leaving behind only the incoherent scattering contribution. So long as the number of PSA iterations is less than the number of scattering pathways, there will be a saving in the computational cost. This condition is easily satisfied (see Results section), making PSA an extremely efficient simulation method.

The generalization to a real system is now straightforward. For phonons, the fundamental multislice formula [equation (1)] in PSA becomes:

$$\Psi_0(\mathbf{R}) = \psi_{\text{inc}}(\mathbf{R}) \quad (7a)$$

$$\begin{aligned}\Psi_n(\mathbf{R}) &= \sum_j P(j)[e^{i\theta_j}\Psi_{n-1}(\mathbf{R})Q_{n,j}(\mathbf{R})] \otimes P_n(\mathbf{R}) \\ &= [\Psi_{n-1}(\mathbf{R})Q_n'(\mathbf{R})] \otimes P_n(\mathbf{R})\end{aligned} \quad (7b)$$

$$Q_n'(\mathbf{R}) = \sum_j P(j)e^{i\theta_j}Q_{n,j}(\mathbf{R}) \quad (7c)$$

where $\psi_{\text{inc}}(\mathbf{R})$ is the incident electron wavefunction determined by the microscope illumination conditions. The summation in equations (7b) and (7c) is over all phonon configurations $j$, which have probability $P(j)$ and phase grating function $Q_{n,j}(\mathbf{R})$ for the $n^{\text{th}}$ slice. $Q_n'(\mathbf{R})$ is an effective phase grating function for the slice. It contains all possible phonon configurations, suitably weighted according to their probability, as well as the random phase angle $\theta_j$ required for incoherence. For correlated atomic motion, $P(j)$ is given by the Bose–Einstein occupation factor (Kittel, 2005). Most frozen phonon calculations however assume uncorrelated atomic motion, for which $P(j)$ is a constant and independent of $j$. Implementation of equations (7b) and (7c) would then require calculating all phase grating functions, $Q_{n,j}(\mathbf{R})$, which does not result in any computational cost saving compared with a standard frozen phonon (SFP) simulation. However, in the MSP method (Peters, 2021), only a small number of frozen phonon configurations are calculated, and the phase grating function for a given slice selected at random from the initial configurations. In this way, many more frozen phonon configurations can be generated without further calculation, the number of possible configurations increasing rapidly with specimen thickness. A multislice simulation must still nevertheless be performed for each new phonon configuration. Therefore, for this part of the simulation, the computation time scales linearly with the number of sampled configurations. With PSA, however, all the possible MSP configurations are sampled simultaneously, with iterations only required to supress the coherent terms in the CBED intensity [equation (4)]. This will be explored in more detail in the Results section.

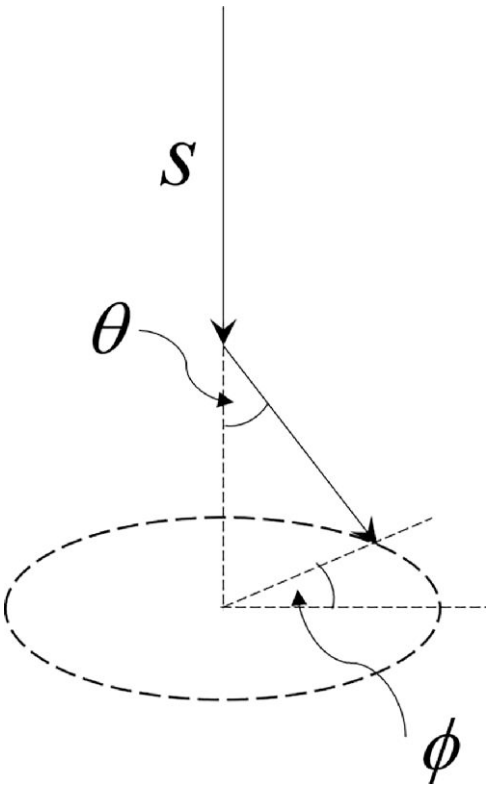


**Fig. 1.** Schematic illustration of a Monte Carlo plasmon scattering event, where $s$ is the path length and $\theta$, $\phi$ are the polar and azimuthal angles of scattering, respectively. $s$, $\theta$, and $\phi$ are estimated from their respective distributions using computer generated random numbers.

We now discuss how PSA can be applied to plasmons. The Monte Carlo plasmon multislice method is illustrated schematically in Figure 1. The electron travels a path length $s$ before undergoing plasmon scattering along polar angle $\theta$ and azimuthal angle $\phi$. The path length and polar angle follow Poisson (Egerton, 1996) and Lorentzian (Ferrell, 1956) distributions, respectively, while the azimuthal angle is randomly distributed over $2\pi$ radians. The scattering parameters $s$, $\theta$, and $\phi$ are estimated using computer-generated random numbers that satisfy the corresponding statistical distributions (Mendis, 2019). The incident electron undergoes a change in transverse wavevector $\Delta\mathbf{k}$ during plasmon excitation, which is equivalent to a phase shift exp $(2\pi i\Delta\mathbf{k}\cdot\mathbf{R})$ in the electron wavefunction (Barthel et al., 2020). Mendis (2019) also considered the effect of beam tilt on the phase grating and propagation functions (Ishizuka, 1982), although for most scattering events, this correction is negligible, since the plasmon characteristic angle $\theta_E$ is much smaller than the Bragg angle (e.g., $\theta_E = 0.04$ mrad for silicon at 200 kV beam voltage). Therefore, in what follows, only the phase shift term in plasmon scattering is retained. The corresponding PSA equations are then:

$$\Psi_0(\mathbf{R}) = \psi_{\text{inc}}(\mathbf{R}) \quad (8a)$$

$$\Psi_n^{\text{source}}(\mathbf{R}) = [\Psi_{n-1}(\mathbf{R})Q_n'(\mathbf{R})] \otimes P_n(\mathbf{R}) \quad (8b)$$

$$Q_n'(\mathbf{R}) = \sum_j P(j)e^{i\theta_j}Q_{n,j}(\mathbf{R}) \quad (8c)$$

$$\begin{aligned}\Psi_n(\mathbf{R}) &= \sqrt{1-P(s)}\Psi_n^{\text{source}}(\mathbf{R}) \\ &+ \sum_{m\in\{s,\theta,\phi\}} \sqrt{P(s)P(\theta)P(\phi)}e^{i\theta_m}e^{2\pi i\Delta\mathbf{k}_m\cdot\mathbf{R}}\Psi_n^{\text{source}}(\mathbf{R})\end{aligned} \quad (8d)$$

The physical interpretation of these equations are as follows. The incident electron wavefunction [equation (8a)] is transmitted and propagated through a slice using the PSA method for frozen phonons [equations (8b) and (8c)]. The resulting wavefunction $\Psi_n^{\text{source}}(\mathbf{R})$ is a source term for plasmon scattering within the thin slice, which is given by equation (8d). The first term on the right-hand side is the unscattered wavefunction, while the summation contains all plasmon scattered wavefunctions. The index $m$ represents the different plasmon scattering configurations (i.e., $s$, $\theta$ and $\phi$ values) with transverse wavevector change $\Delta\mathbf{k}_m$. $\theta_m$ is the randomly generated phase angle for maintaining incoherence. $P(s)$ is the probability for plasmon scattering between path lengths $s$ and $s + ds$, and similarly for $P(\theta)$ and $P(\phi)$. It can be shown that (Mendis, 2019):

$$P(s) = \exp\left(-\frac{s}{\lambda_p}\right)\frac{ds}{\lambda_p} \tag{9a}$$

$$P(\theta) = \frac{2\theta d\theta}{(\theta^2 + \theta_E^2)\ln[1 + (\theta_c/\theta_E)^2]} \tag{9b}$$

$$P(\phi) = \frac{d\phi}{2\pi} \tag{9c}$$

where $\lambda_p$ is the plasmon mean free path and $\theta_c$ is the critical angle for plasmon damping (Egerton, 1996). The probability that the incident electron does not excite a plasmon within a given slice is $1 - P(s)$. The unscattered wavefunction in equation (8d) however contains a $\sqrt{1 - P(s)}$ term, since the electron density is given by the square modulus of the wavefunction. Similar considerations apply to the $\sqrt{P(s)P(\theta)P(\phi)}$ factor in equation (8d). The total wavefunction $\Psi_n(\mathbf{R})$ is transmitted and propagated through the next slice using equations (8b) to (8c), before undergoing further plasmon scattering within the new slice [equation (8d)]. This process is repeated until the exit surface is reached (the small effect of plasmon energy loss on transmission and propagation of the high energy electron beam is ignored). Note that equation (8d) models only single plasmon scattering events within a given slice. This is reasonable, since the slice thickness is much smaller than the plasmon mean free path (e.g., 105 nm for silicon at 200 kV beam voltage).

It is easy to see that equations 8a–8d include multiple plasmon scattering within the specimen as well. In fact, the resulting CBED pattern is similar to the energy unfiltered diffraction patterns measured in most experiments. It is possible however to also simulate energy filtered CBED patterns. For example, consider the single plasmon energy CBED pattern. Equation (8d) must be replaced with two separate wavefunctions:

$$\Psi_n^p(\mathbf{R}) = \sum_{m\in\{s,\theta,\phi\}} \sqrt{P(s)P(\theta)P(\phi)}e^{i\theta_m}e^{2\pi i\Delta\mathbf{k}_m\cdot\mathbf{R}}\Psi_n^{\text{source}}(\mathbf{R}) \tag{10a}$$

$$\Psi_n(\mathbf{R}) = \sqrt{1 - P(s)}\Psi_n^{\text{source}}(\mathbf{R}) \tag{10b}$$

$\Psi_n^p(\mathbf{R})$ consists of the single scatter plasmon wavefunctions generated within slice $n$. It is transmitted and propagated through the rest of the crystal without any further plasmon scattering. The phonon PSA equations (7b) and (7c) are used for this purpose. This gives the contribution of slice $n$ to the single plasmon energy CBED pattern. To determine the contribution from other slices, we only retain the wavefunction that has not undergone plasmon scattering [equation (10b)] and repeat the process of transmission, propagation [equations (8b) and (8c)], and plasmon scattering [equation (10a)] until the specimen exit surface is reached. The final CBED pattern is obtained by incoherently summing single plasmon scattering contributions from all the slices. It is also possible to calculate double and higher-order plasmon energy CBED patterns along similar lines, although at an increasing computational cost and complexity. In fact, an energy unfiltered CBED calculation [equations (8a)–(8d)] is by far the most efficient plasmon scattering simulation to perform.

## Simulation Method

Silicon is used as a test specimen for PSA since it has distinct plasmon peaks with no interband transitions in the low electron energy loss region, and because experimental data is available in the literature (Mendis, 2019, Barthel et al., 2020). Phonon PSA was performed on 50 nm thick [100]-Si, with the simulation cell having lateral dimensions of $10a_o \times 10a_o$ (i.e., 54.3 Å × 54.3 Å), where $a_o$ is the unit cell lattice parameter. The slice thickness was ($a_o$/4) or 1.4 Å. The projected potential for a given slice was calculated using Kirkland's (2010) atom scattering factors, at 1024 × 1024 pixel sampling. Frozen phonons were generated assuming uncorrelated atom motion, and a root mean square atomic displacement of 0.078 Å (Kirkland, 2010). The MSP method (Peters, 2021) is used for calculating frozen phonons. There are four crystallographically distinct slices in [100]-Si. For each of these crystallographic slices, five or ten frozen phonon configurations were generated and stored in computer memory. These are later used for calculating the effective phase grating function [equations (7c) and (8c)]. Since the phonon probability $P(j)$ is a constant for uncorrelated atom motion, it can effectively be ignored (see also the comments on wavefunction normalization at the end of this section). The STEM probe parameters were 200 kV accelerating voltage, 4 mrad semi-convergence angle and no electron optic aberrations. The STEM probe was positioned at the center of the (projected) supercell; see Supplementary Material.

Plasmon PSA was performed on a 50 nm thick, [110]-Si simulation cell with lateral dimensions of $7\sqrt{2}a_o \times 10a_o$ (53.8 Å × 54.3 Å). The [110] orientation was chosen because experimental plasmon data is available for this zone-axis (Mendis, 2019). There are two crystallographically distinct slices for [110]-Si, each with slice thickness $\sqrt{2}a_o/4$ or 1.9 Å. Five frozen phonon configurations were constructed for these distinct slices using the same MSP procedure as [100]-Si. The plasmon scattering parameters are 1050 Å mean free path ($\lambda_p$), 0.04 mrad characteristic angle ($\theta_E$) and 19.1 mrad critical angle ($\theta_c$). $\lambda_p$ was measured directly (Mendis, 2019) and $\theta_c$ was obtained by fitting simulation to experiment (Barthel et al., 2020; the $\theta_c$ value used here is adjusted for the difference in accelerating voltage between the two investigations, i.e., 200 versus 300 kV). $\theta_E$ was calculated from $\Delta E/2E_o$, where $\Delta E$ is the plasmon energy loss and $E_o$ the primary beam energy (Egerton, 1996).

The plasmon phase shift, $\exp(2\pi i\Delta\mathbf{k}_m \cdot \mathbf{R})$, can be conveniently applied in reciprocal space, using the Fourier shift theorem. The shifting does however introduce artifacts when inverse Fourier transforming back to real space. This can be minimized by applying a Hanning window, as well as rounding $\Delta\mathbf{k}_m$ to integer multiples of the pixel size ($k_{\text{pixel}}$) in reciprocal space (Barthel et al., 2020). The latter also determines the

discrete sampling for the plasmon scattering angles $\theta$ and $\phi$. First consider the polar angle $\theta$. The smallest polar scattering angle $\theta_{\text{min}}$ is given by $k\theta_{\text{min}} \sim k_{\text{pixel}}$, where $k$ is the wavenumber of the incident electrons. In principle, the polar scattering angle should be sampled in step sizes of $\theta_{\text{min}}$ up to the critical angle $\theta_c$. However, since $\theta_c \gg \theta_E$, the plasmon scattering probability at these very high angles is negligible. Furthermore, large scattering angles are also more susceptible to the inverse Fourier transform artifacts discussed earlier. Therefore, the maximum polar scattering angle $\theta_{\text{max}}$ is limited to $5\theta_{\text{min}}$, i.e. 2.3 mrad, which is still nevertheless significantly larger than $\theta_E$ (0.04 mrad). Note that $\theta_{\text{min}}$ is much coarser than $\theta_E$, but still only a fraction of the Bragg angle. The sampling of $\theta$ is therefore appropriate, in the sense that scattering angles of the order of $\theta_E$ do not significantly affect channeling of the incident electron beam, although the probability of scatter $P(\theta)$ will be inaccurate [equation (9b)]. Using the formula for an arc length in a circle, the minimum azimuthal scattering angle $\phi_{\text{min}}$ is given by $(k\theta_{\text{max}})\phi_{\text{min}} \sim k_{\text{pixel}}$. The azimuthal angle is sampled over $2\pi$ radians in step sizes of $\phi_{\text{min}}$ (i.e., 0.2 rad).

The Fourier shift method resulted in a large increase in the simulation time. A more efficient procedure for calculating the plasmon phase shifts was therefore required. Consider all plasmon scattering events within a given slice at fixed polar angle, i.e. constant $s$ and $\theta$. The summation term in equation (8d) for these plasmon events is:

$$\sqrt{P(s)P(\theta)}\left[\sum_{\phi}\sqrt{P(\phi)}e^{i\theta_m}e^{2\pi i\Delta\mathbf{k}_m\cdot\mathbf{R}}\right]\Psi_n^{\text{source}}(\mathbf{R}) \qquad (11)$$

Instead of random values for the phase scrambling angle $\theta_m$, let us assume that:

$$e^{i\theta_m} = \frac{e^{in\phi}}{i^n} \qquad (12)$$

where $n$ is any positive real number. The phase scrambling angle is a function of $\phi$, and therefore varies somewhat with the plasmon configuration $m$, the exception being configurations with the same $\phi$ value. However, the phase angle is not truly random, since it must also satisfy equation 12. Therefore, $\theta_m$ is best described as being pseudo-random. Substituting equations 9c and 12 in equation 11 gives:

$$\sum_{\phi}\sqrt{P(\phi)}e^{i\theta_m}e^{2\pi i\Delta\mathbf{k}_m\cdot\mathbf{R}} = \sqrt{\frac{2\pi}{\Delta\phi}}\sum_{\phi}\frac{e^{i(n\phi+2\pi k\theta R\cos\phi)}}{2\pi i^n}\Delta\phi \qquad (13)$$

where $k\theta$ is the magnitude of the transverse wavevector $\Delta\mathbf{k}_m$. $\Delta\phi$ is equal to the azimuthal angle step size $\phi_{\text{min}}$. Assuming $\phi_{\text{min}}$ is infinitesimally small, the summation on the right-hand side of equation 13 can be replaced with an integral, i.e.

$$\begin{aligned}\sum_{\phi}\sqrt{P(\phi)}e^{i\theta_m}e^{2\pi i\Delta\mathbf{k}_m\cdot\mathbf{R}} &\rightarrow \sqrt{\frac{2\pi}{\phi_{\text{min}}}}\int_0^{2\pi}\frac{e^{i(n\phi+2\pi k\theta R\cos\phi)}}{2\pi i^n}d\phi \\ &= \sqrt{\frac{2\pi}{\phi_{\text{min}}}}J_n(2\pi k\theta R)\end{aligned} \qquad (14)$$

where $J_n$ is a Bessel function of the first kind. With the aid of equation 14, the summation in equation (8d) must now only be carried out over $\theta$ for any given slice. Unfortunately, there does not appear to be a simple analytical solution for this part of the calculation, which was therefore done numerically. Nevertheless, there is still a significant saving in computational cost, since for our simulations the number of sampling points for $\phi$ is larger than $\theta$ by a factor of 28. For a given slice and polar angle $\theta$, the order $n$ of the Bessel function was randomly chosen. In principle, $n$ can be any number between zero and infinity. However, as a *general* trend, $J_n(2\pi k\theta R)$ decreases to zero with increasing $n$. For our simulations, $J_n(2\pi k\theta R)$ was zero for the full range of $2\pi k\theta R$ values provided that $n > 30$. Therefore, $n$ was randomly varied between 0 and 30. A further reduction in computing time is achieved by pre-calculating a few Bessel functions for each value of θ at the start of a PSA iteration, and then substituting these at random for any given slice. This is similar to the MSP method, except here it is the Bessel functions that are being calculated, rather than phase grating functions. Five Bessel functions were calculated for each of the five different θ values between zero and $\theta_{\text{max}}$ at the start of each PSA iteration.

It was previously mentioned that the wavefunction in equation (3) is not normalized. This is also the case for the PSA wavefunctions for phonons [equation (7b)] and plasmons [equation (8d)]. Mathematically, this is a trivial issue, since we are interested in only the incoherent part of the CBED intensity $I(\mathbf{k})$, e.g. equation (4). The sum $\sum I(\mathbf{k})$ from a sufficiently large number of PSA iterations will be free of cross-terms, and therefore strictly proportional to the incoherent intensity. However, it was found that $\sum I(\mathbf{k})$ rapidly increased to values that were too large to store in computer memory, especially for reasonably thick specimens (e.g., 50 nm) where there are a large number of scattering pathways. To avoid this, the exit wavefunction after each PSA iteration was normalized, so that $\sum I(\mathbf{k})$ remained bounded. Strictly speaking, in order for the cross-terms to exactly cancel, the wavefunction should not be normalized. The resulting error causes some quantitative disagreement between PSA and conventional multislice simulations (see Fig. 4b). It should nevertheless be emphasized that normalization is not an intrinsic requirement of PSA, but rather is imposed by limitations in computer hardware. The PSA was coded in MATLB and the simulations run on a standard desktop PC with 8 GB RAM. The simulation run time was determined using the MATLAB "tic toc" command.

## Results and Discussion

### Phonon Phase Scrambling

In order to test the accuracy of phonon PSA, reference data from the more established simulation methods are first required. Figure 2a shows the CBED pattern for a 50 nm thick, [100]-Si specimen after 100 SFP iterations. For visual clarity, all CBED patterns are displayed using a logarithmic intensity scale, and only the central half of the diffraction pattern, where scattering is strongest, is shown. The SFP is the most accurate phonon simulation method considered here, although it is also by far the most computationally demanding (the simulation time for Fig. 2a was several days). Figures 2b and 2c show the same CBED pattern calculated using the MSP method (100 iterations), with five and ten pre-calculated frozen phonon configurations for each of the four crystallographically distinct slices, respectively. The MSP can be inaccurate if there are too few starting phonon configurations (Peters, 2021). Convergence between Figures 2b and 2c was quantified by plotting the average radial intensity profiles as a function of

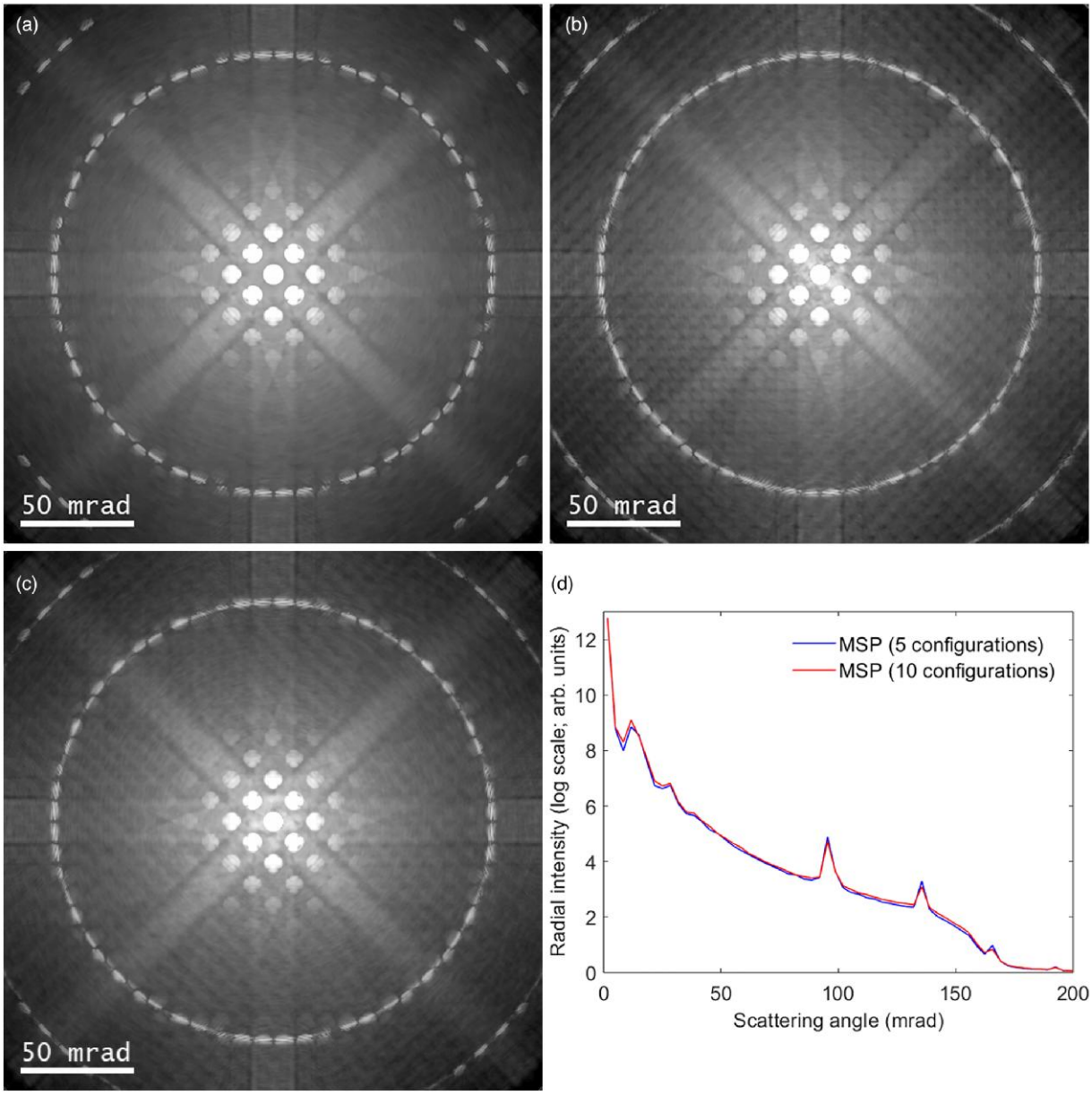


**Fig. 2.** 50 nm specimen thickness, [100]-Si convergent beam electron diffraction (CBED) patterns for (**a**) standard frozen phonon, and mixed static potential simulations with (**b**) five and (**c**) ten starting phonon configurations per crystallographic slice. Each diffraction pattern is the incoherent sum of 100 iterations. Plasmons were not included in the simulations. The CBED patterns are displayed on a logarithmic intensity scale. (**d**) plots the average radial intensity profiles for the CBED patterns in (**b**) and (**c**).

scattering angle (Fig. 2d). The abrupt drop in intensity at around 150 mrad is caused by the multislice bandwidth limit (157 mrad; Kirkland, 2010). The strong overlap of the two intensity profiles indicates that five starting phonon configurations are sufficient for this particular example. The MSP reproduces the gross features (Kikuchi bands, higher-order Laue zone (HOLZ) rings etc.) observed in the SFP result, although there are also subtle differences. For example, MSP has a more textured background, which is likely due to the limited number of starting phonon configurations, since it appears more strongly in Figure 2b compared with Figure 2c. It should be emphasized that these differences are only apparent when the intensity is plotted on a logarithmic scale. The slight inaccuracy of MSP is offset by a massive reduction in simulation time from days to minutes.

Phonon PSA simulations for the same specimen were carried out using five phonon starting configurations, and the results after 1, 10, 50, and 100 PSA iterations are shown in Figures 3a to 3d, respectively. Recall that PSA simulates all scattering pathways simultaneously. For a 50 nm thick specimen (368 slices) and five starting phonon configurations, there are a total of $5^{368}$ possible scattering pathways, an astronomically large number. Despite this, the PSA result after one iteration is extremely noisy, and although Bragg discs and HOLZ rings are present, Kikuchi bands from thermal diffuse scattering are less well defined (Fig. 3a). This is nevertheless consistent with the results of Forbes et al. (2010; see Figs. 2, 3 of their paper), where it was shown that only coherent Bragg scattering remains after coherent superposition of the exit wavefunctions for different frozen phonon configurations. In Figure 3a,

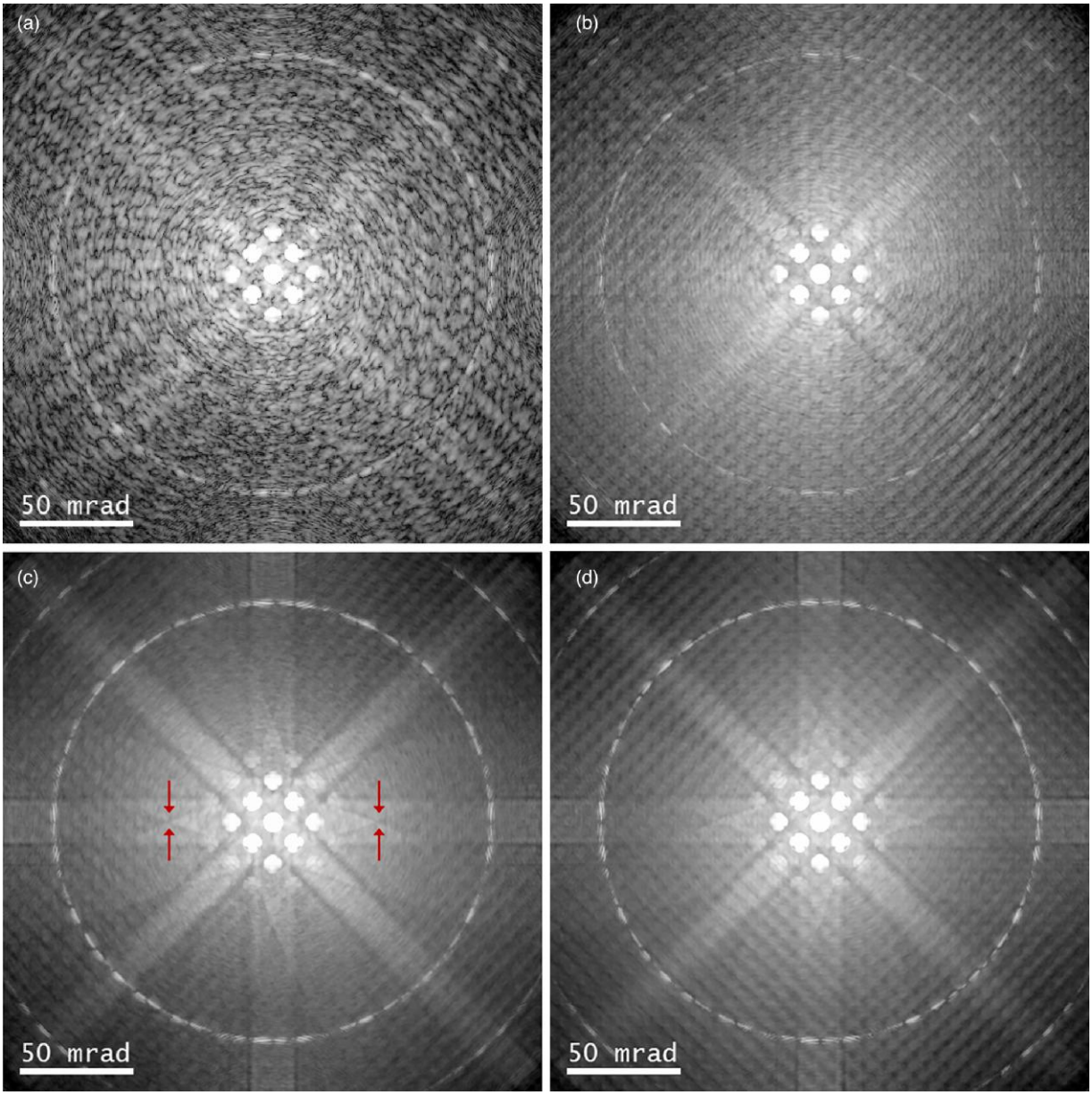


**Fig. 3.** Phonon phase scrambling algorithm (PSA) simulation results for the convergent beam electron diffraction pattern (logarithmic intensity scale) in a 50 nm thick, [100]-Si specimen after (**a**) 1, (**b**) 10, (**c**) 50, and (**d**) 100 PSA iterations. Five starting phonon configurations were used per crystallographic slice. Plasmon scattering is not included. The arrows in (**c**) mark the location of intersecting higher order Kikuchi lines.

only one iteration of phase scrambling has been applied, and there is still a high degree of coherence between the different phonon scattered wavefunctions. Therefore, Kikuchi bands, which rely on incoherent scattering, are only weakly present. The residual coherence becomes progressively suppressed with increasing number of PSA iterations (Figs. 3b–3d), and consequently there is more contrast in the Kikuchi bands. After 50 iterations, subtle features, such as higher-order intersecting Kikuchi lines (see arrows in Fig. 3c), are reproduced, consistent with the SFP result (Fig. 2a). By 100 iterations, however, the textured background, which was previously observed with MSP, is apparent in PSA as well (Fig. 3d). Since PSA samples all possible scattering pathways, the appearance of texture is likely an artifact of the limited number of starting phonon configurations, and thus highlights an intrinsic limitation of the MSP method for generating new frozen phonon configurations that are sufficiently distinct from one another.

Figure 4a plots the average CBED radial intensity profiles for different number of PSA iterations. The profile converges after ~50 iterations. In Figure 4b, the average radial intensity profile after 100 PSA iterations is compared with the SFP and MSP results for the same number of iterations (Figs. 2a, 2b, respectively). There is good agreement between SFP and MSP, but the PSA intensity is higher for scattering angles larger than ~5 mrad. This implies that the electron flux is not conserved. In all simulations, the integrated intensity in the real space exit wavefunction was normalized before multiplying by a Hanning window (to reduce aliasing artifacts) and Fourier transforming to obtain the CBED pattern. The Hanning window may have affected the integrated intensity in the diffraction pattern, giving rise to the anomaly in

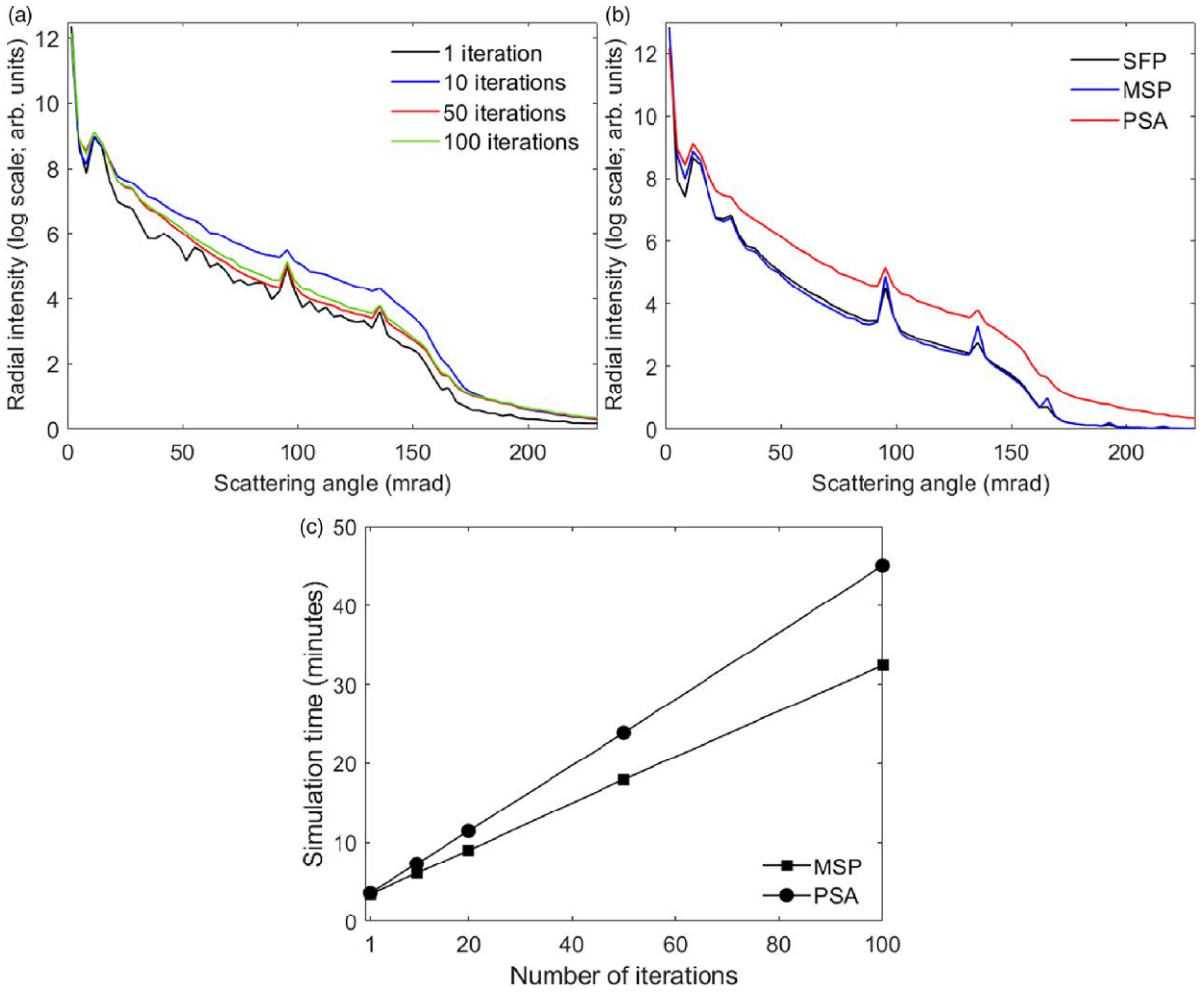


**Fig. 4.** (**a**) Average radial intensity profiles for the convergent beam electron diffraction (CBED) patterns in Figure 3. (**b**) is a comparison of the average radial intensity profiles for the standard frozen phonon (SFP) and mixed static potential (MSP) results in Figures 2a and 2b, and the phase scrambling algorithm (PSA) result in Figure 3d. These are converged CBED patterns, each with 100 iterations. (**c**) is a plot of the simulation times for phonon PSA and MSP calculations in a 50 nm thick, [100]-Si specimen as a function of number of iterations. For each data point, there were five starting phonon configurations per crystallographic slice.

Figure 4b. This would especially be true for thicker specimens, such as the 50 nm thick silicon sample used here, where scattering of the electron probe is more severe. The HOLZ rings at 95 and 135 mrad scattering angle are also sharper in SFP and MSP compared with PSA (Fig. 4b). Furthermore, higher-order Bragg reflections are weaker in PSA (Fig. 3d) compared with SFP (Fig. 2a) and MSP (Fig. 2b). These trends are consistent with a larger Debye–Waller factor for PSA. Therefore, while PSA does give satisfactory results, subtle differences still remain compared with conventional simulation routines, such as SFP. It is difficult to identify the exact cause(s) of the discrepancy, especially since the differences are at the lower end of the CBED pattern intensity, which has a large dynamic range.

Finally, consider the time required for PSA simulation. Figure 4c plots the simulation time for MSP and PSA as a function of number of iterations. Both simulation methods have an initial computational cost for calculating the starting phonon configurations (five configurations per crystallographic slice). Once this is completed, the simulation time increases linearly with the number of iterations. The simulation time for PSA is higher because a more complex phase grating function [equation (7c)] must be calculated. Nevertheless, the gradient of the trend line for PSA is steeper by only a factor of ~1.4 compared with MSP (Fig. 4c). The moderate increase in simulation time could be justified by the large increase in scattering pathways that are modeled, i.e. $5^{368}$ for PSA versus 100 (maximum) for MSP. However, for most applications, a few tens of phonon configurations are sufficient to give accurate results, and therefore, such a large number of phonons may not be required. Furthermore, from Figure 4b, phonon PSA results are not as accurate as other multislice methods, such as MSP and SFP.

## Plasmon Phase Scrambling

Plasmon PSA was tested on a 50 nm thick, [110]-Si specimen. Equations (8a) to (8d) were used to simulate energy unfiltered CBED patterns, which contained both phonon and multiple plasmon scattering. Five phonon configurations for each of the two crystallographically distinct slices were pre-calculated at the start of the multislice simulation. The Bessel pseudo-random method was used for plasmon calculations, with five Bessel functions ($0 \leq n \leq 30$) for each plasmon polar scattering

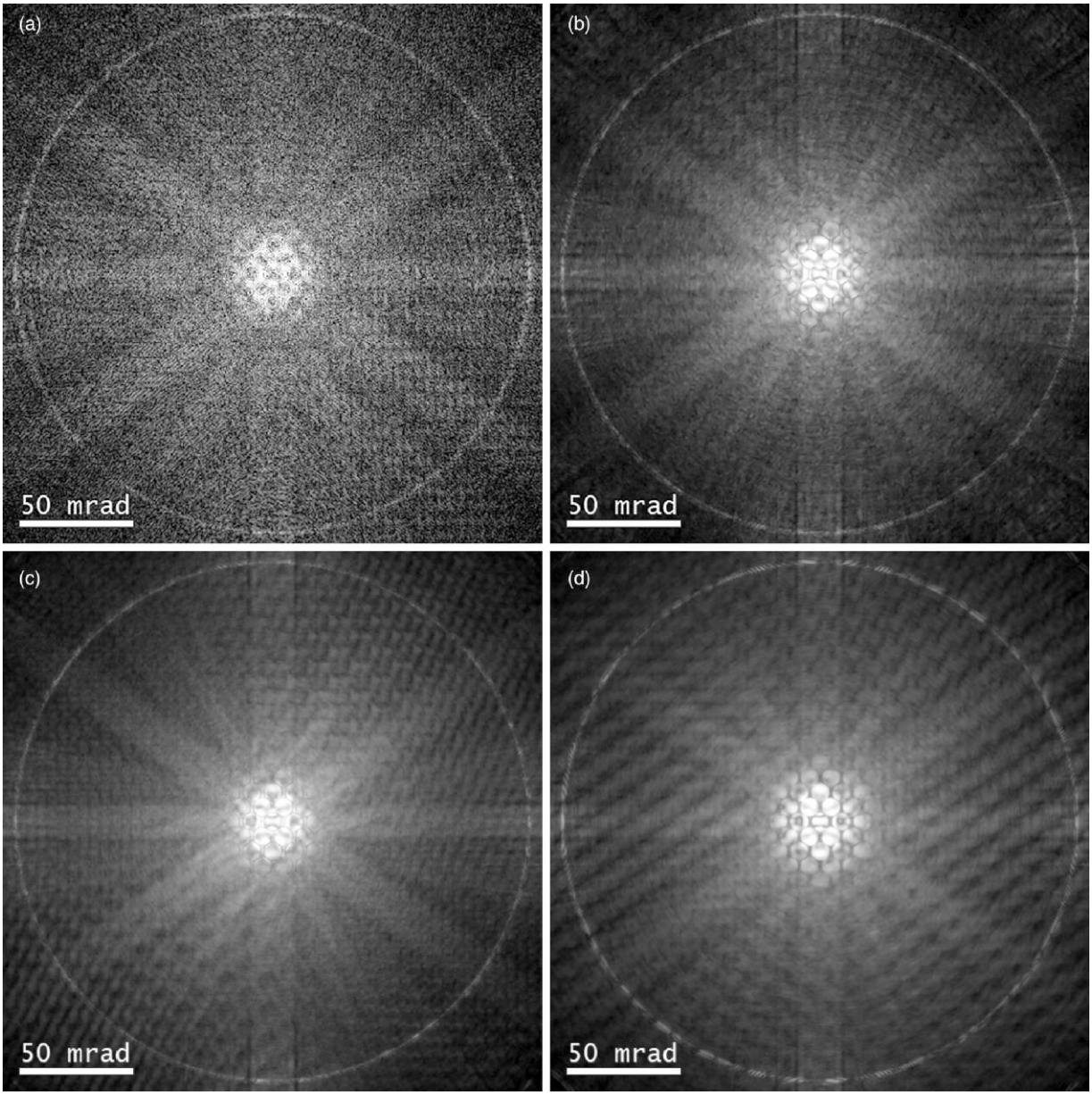


**Fig. 5.** Plasmon phase scrambling algorithm (PSA) simulation results for the energy unfiltered convergent beam electron diffraction (CBED) pattern in a 50 nm thick, [110]-Si specimen after (**a**) 1, (**b**) 20, and (**c**) 50 iterations of the Bessel pseudo-random method. Five phonon configurations were used for each crystallographic slice, and five Bessel functions for each plasmon polar scattering angle were calculated at the start of every PSA iteration. (**d**) shows the energy unfiltered CBED pattern for the same sample calculated using the Fourier shift method (50 iterations and 5 starting phonon configurations). The CBED patterns are displayed on a logarithmic intensity scale.

angle θ calculated at the start of every PSA iteration. Figures 5a to 5c show the results for 1, 20, and 50 PSA iterations, respectively. The Kikuchi bands after one PSA iteration show very little contrast due to residual coherence, similar to the phonon only calculation in Figure 3a. However, the introduction of plasmons has also suppressed the intensity in the transmitted and Bragg diffracted discs. This is likely caused by the phase shift term $\exp(2\pi i \Delta \mathbf{k}_m \cdot \mathbf{R})$ in equation (8d), and because there is a high degree of coherence between elastic and plasmon scattered wavefunctions. Multiple PSA iterations progressively suppresses the coherence, resulting in higher contrast Kikuchi bands and Bragg discs. The average radial intensity profiles in Figure 6a converge rapidly with number of PSA iterations. There was very little change to the profile between 50 and 100 iterations. Therefore, 50 iterations were used for all future simulations, and the results assumed to have been converged. Note that some texturing in the background intensity is visible in Figure 5c, which is also seen in the phonon only simulation (Fig. 7a), and therefore attributed to the limited number of starting phonon configurations.

Figure 5d shows the energy unfiltered CBED pattern (50 iterations) calculated using the Fourier shift method. This is computationally slower, but in principle more accurate than the Bessel pseudo-random method, since truly random numbers are used for the phase scrambling. The CBED patterns calculated with the two methods show subtle differences in the fine structure. For example, the higher-order Bragg reflections have lower intensity in the Bessel pseudo-random result.

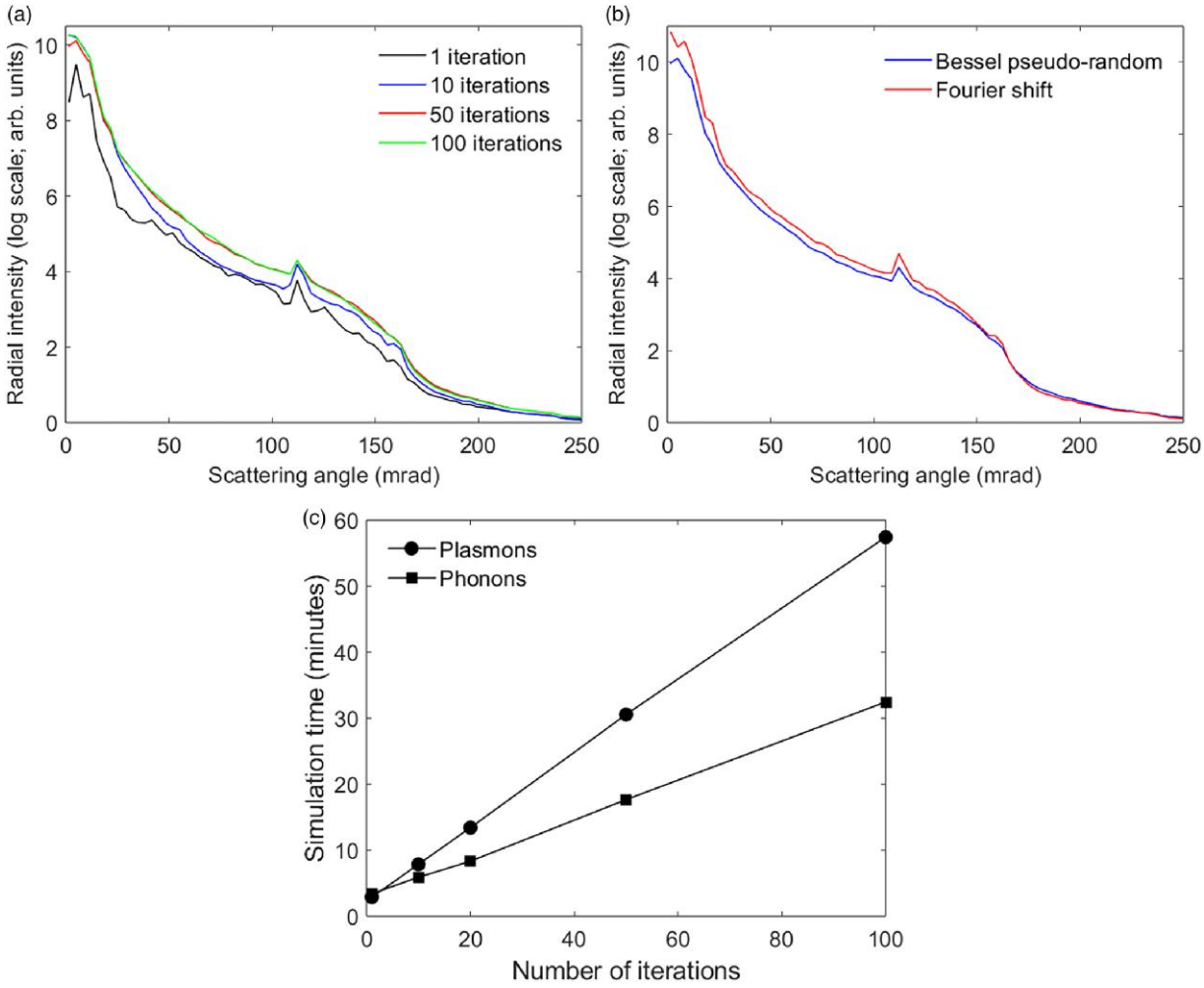


**Fig. 6.** (**a**) Average radial intensity profiles for the plasmon phase scrambling algorithm (PSA) convergent beam electron diffraction (CBED) patterns in Figure 5. (**b**) is a comparison of the average radial intensity profiles for the Bessel pseudo-random and Fourier shift results in Figures 5c and 5d. (**c**) is a plot of the simulation times for plasmon and phonon PSA calculations in a 50 nm, [110]-Si specimen as a function of number of PSA iterations. The Bessel pseudo-random method was used for the plasmon PSA simulations, with five Bessel functions calculated at the start of each PSA iteration for every plasmon polar scattering angle. For each data point, there were five starting phonon configurations per crystallographic slice.

The average radial intensity profiles for the two methods (Fig. 6b) are different at scattering angles smaller than ~160 mrad, although the relative difference is no more than 8.3%. The inaccuracy is larger for thicker specimens, where plasmon excitation is more likely (see Supplementary Material). Furthermore, increasing the number of pre-calculated Bessel functions from five to ten did not lead to an improvement in accuracy (see Supplementary Material).

The main advantage of the Bessel method, however, is its computational efficiency. As an example, the Fourier shift result in Figure 5d required a simulation time of 6 h, compared with only 30 min for Bessel pseudo-random (Fig. 5c), an order of magnitude increase in speed. In Figure 6c, the simulation time for Bessel pseudo-random plasmon PSA is compared with phonon PSA. The gradient of the trend line for plasmons is steeper by a factor of 1.9, a near doubling of the computational cost compared with phonons for large number of iterations. Nevertheless, this still represents a significant time saving compared with the traditional Monte Carlo method for plasmons, where tens of thousands of multislice simulations must be performed for convergence (Barthel et al., 2020, Mendis, 2022*a*).

Finally, consider the energy dependence of the CBED patterns. Figure 7a is the phonon PSA result for a 50 nm thick specimen of [110]-Si. Equations (7a) to (7c) were used for the calculation, which consisted of 50 PSA iterations and five starting phonon configurations for each of the two crystallographically distinct slices. Since only phonons are included, the result is equivalent to a zero-loss peak (ZLP) filtered CBED pattern measured in most microscopes with limited energy resolution. Figure 7a is similar to the energy unfiltered CBED pattern (Fig. 5d), which is to be expected, since from Poisson statistics, 62% of the incident electrons have not undergone any plasmon scattering. Figures 7b and 7c are the single plasmon energy CBED patterns, calculated by applying Bessel pseudo-random and Fourier shift methods in equations 10a to 10b, respectively. In addition to the pre-calculated phonon configurations, the former method also used five Bessel functions for each $\theta$ angle, which were calculated at the start of every PSA iteration.

The Bessel pseudo-random and Fourier shift methods produce very different single plasmon CBED patterns. For example, compared with the ZLP filtered CBED pattern, the contrast of Kikuchi bands, intersecting Kikuchi lines and

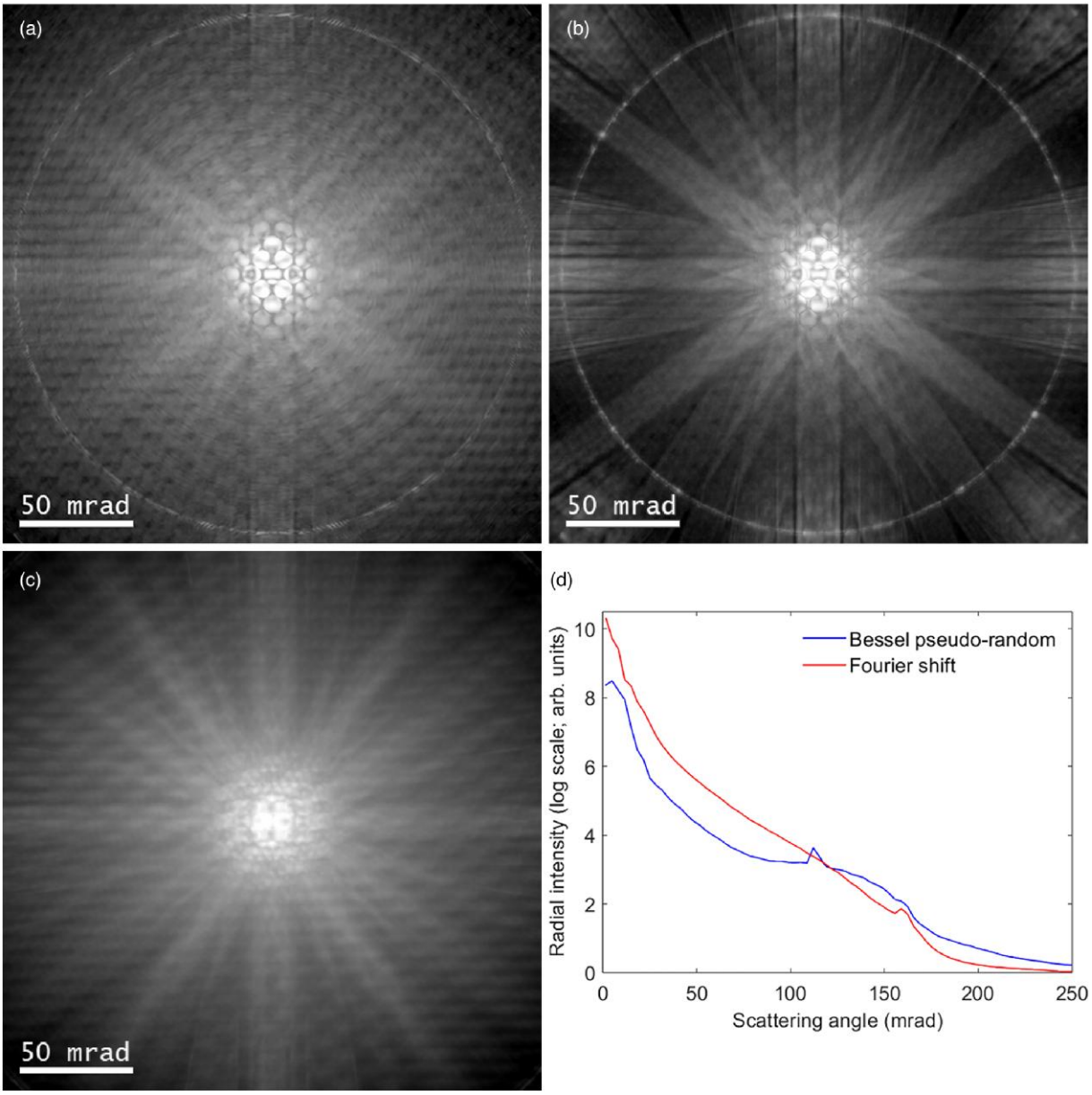


**Fig. 7.** (**a**) Zero loss peak filtered convergent beam electron diffraction (CBED) pattern for a 50-nm thick, [110]-Si specimen calculated using phonon PSA. (**b**) and (**c**) are the CBED patterns for the same specimen at single plasmon energy loss, calculated using Bessel pseudo-random and Fourier shift plasmon PSA methods, respectively. The CBED patterns are displayed on a logarithmic intensity scale. Five phonon configurations were used for each crystallographic slice, and for the Bessel pseudo-random method five Bessel functions for each plasmon polar scattering angle were calculated at the start of every PSA iteration. (**d**) plots the average radial intensity profiles for the CBED patterns in (**b**) and (**c**).

HOLZ rings, is higher for the Bessel pseudo-random method (Fig. 7b). However, for the Fourier shift result (Fig. 7c), the diffracted discs, Kikuchi bands and lines are blurred, while the HOLZ ring has completely disappeared. The average radial intensity profiles (Fig. 7d) also highlight significant quantitative differences between the two simulation methods. Experimental results for [110]-Si indicate that diffracted discs and Kikuchi bands become blurred with plasmon scattering (Mendis, 2019); unfortunately, the camera length in that study was too large to capture the HOLZ rings, and therefore no comment can be made about their contrast. This blurring is caused by a plasmon de-channeling effect (Mendis, 2019), and has been reported for other materials besides silicon, such as platinum (Beyer et al., 2020) and aluminum (Robert et al., 2022). The experimental observations are consistent with the Fourier shift result, although the degree of blurring is stronger in simulation. For example, experiment indicates that multiple plasmon excitations are required to noticeably reduce the contrast in an energy filtered CBED pattern (see Figs. 3, 4 in Mendis, 2019), while for simulation, a single plasmon scattering event is sufficient. This may be due to an underestimation of the critical angle $\theta_c$ in the simulations, so that the plasmon scattering probability at a given polar angle [equation (9b)] is higher than what it should be. Plasmon dispersion (Egerton, 1996) could also result in deviations from the simple Lorentzian scattering model considered here. Whatever the reason, it is clear that the Fourier shift result is consistent with physical reality, while the Bessel pseudo-random method

for calculating single plasmon CBED, patterns must be treated with caution.

## Summary and Conclusions

In this work, a multislice PSA that models all inelastic scattering paths simultaneously is proposed, with phase scrambling used to maintain incoherence between the inelastic scattering events. This approach is different from conventional multislice techniques, where individual inelastic scattering paths are simulated one at a time. The PSA thus avoids the need to perform an excessively large number of multislice iterations. This is especially beneficial for plasmon scattering, where the number of iterations is reduced from tens of thousands to only a few tens of iterations. Bessel pseudo-random phase scrambling can also be used to further speed up plasmon simulations at the expense of some accuracy, although care must be taken when applying to energy-filtered CBED patterns. For the simulation parameters considered here, plasmon PSA nearly doubled the simulation time compared with a phonon only PSA. The extra computational cost for plasmons can be made smaller by reducing the number of iterations and/or precalculated Bessel functions, provided compromises are made on the desired level of accuracy. Furthermore, the simulation times reported in this work are far from being optimized; further improvements in performance are achieved using compiled computer codes (MATLAB is an interpreted language) and more powerful hardware. Since plasmon PSA includes multiple inelastic scattering, the results are similar to energy unfiltered data obtained during routine measurements, and are therefore more appropriate for a quantitative comparison with experiment. Several recent reports (Barthel et al, 2020, Beyer et al., 2020, Grieb et al., 2022, Robert et al., 2022) highlight the importance of inelastic scattering for accurately modeling experimental data.

The computational efficiency of PSA opens up the possibility of simulating large 4D STEM datasets. PSA is compatible with the PRISM simulation method of Ophus (2017), and there are major gains to be achieved by combining the two. Furthermore, the general PSA approach is applicable to other collective excitations, such as magnons (Lyon et al., 2021, Mendis, 2022*b*), as well as core-loss inelastic scattering. For example, in energy dispersive X-ray (EDX) mapping, the X-ray signal depends on the square modulus of the real space electron wavefunction, $|\Psi(\mathbf{R})|^2$, within the specimen. This is a similar problem to calculating the CBED intensity in reciprocal space, and therefore, a real space version of PSA can easily be constructed for STEM EDX. Channeling of an atomic scale electron beam in a crystalline specimen has a strong influence on the measured EDX concentrations (MacArthur et al., 2021); fast and accurate simulations are therefore indispensable for correct interpretation of experimental data.

## Supplementary Material

To view supplementary material for this article, please visit https://doi.org/10.1093/micmic/ozad052.

## Acknowledgments

I would like to thank Colin Ophus for stimulating discussions that inspired this work.

## Financial Support

The current study has not received any funding from any organizations or institutions.

## Conflict of Interest

The authors declare that they have no competing interest.

## References

Barthel J, Cattaneo M, Mendis BG, Findlay SD & Allen LJ (2020). Angular dependence of fast-electron scattering from materials. *Phys Rev B* **101**, 184109. https://doi.org/10.1103/PhysRevB.101.184109

Beyer A, Krause FF, Robert HL, Firoozabadi S, Grieb T, Kükelhan P, Heimes D, Schowalter M, Müller-Caspary K, Rosenauer A & Volz K (2020). Influence of plasmon excitations on atomic-resolution quantitative 4D scanning transmission electron microscopy. *Sci Rep* **10**, 17890.

Buxton BF, Eades JA, Steeds JW & Rackham GM (1976). The symmetry of electron diffraction zone axis patterns. *Philos Trans R Soc A* **281**, 171–194.

Cowley JM & Moodie AF (1957). The scattering of electrons by atoms and crystals. *I A new heoretical Approach Acta Cryst A* **10**, 609–619.

Egerton RF (1996). *Electron Energy-Loss Spectroscopy in the Electron Microscope*. New York: Plenum Press.

Ferrell RA (1956). Angular dependence of the characteristic energy loss of electrons passing through metal foils. *Phys Rev*. **101**, 554–563. https://doi.org/10.1103/PhysRev.101.554

Findlay SD, Shibata N, Sawada H, Okunishi E, Kondo Y & Ikuhara Y (2010). Dynamics of annular bright field imaging in scanning transmission electron microscopy. *Ultramicroscopy* **110**, 903–923. https://doi.org/10.1016/j.ultramic.2010.04.004

Forbes BD, Martin AV, Findlay SD, D'Alfonso AJ & Allen LJ (2010). Quantum mechanical model for phonon excitation in electron diffraction and imaging using a born-oppenheimer approximation. *Phys Rev B* **82**, 104103. https://doi.org/10.1103/PhysRevB.82.104103

Grieb T, Krause FF, Müller-Caspary K, Ahl JP, Schowalter M, Oppermann O, Hertkorn J, Engl K & Rosenauer A (2022). Angle-dependence of ADF-STEM intensities for chemical analysis of InGaN/GaN. *Ultramicroscopy* **238**, 113535. https://doi.org/10.1016/j.ultramic.2022.113535

Hirsch PB, Howie A, Nicholson RB, Pashley DW & Whelan MJ (1965). *Electron Microscopy of Thin Crystals*. Great Britain: Butterworths.

Ishizuka K (1982). Multislice formula for inclined illumination. *Acta Cryst A* **38**, 773–779. https://doi.org/10.1107/S0567739482001594

Kirkland EJ (2010). *Advanced Computing in Electron Microscopy*, 2nd ed. New York: Springer.

Kittel C (2005). *Introduction to Solid State Physics*, 8th ed. USA: John Wiley and Sons.

Loane RF, Xu P & Silcox J (1991). Thermal vibrations in convergent-beam electron diffraction. *Acta Cryst. A* **47**, 267–278. https://doi.org/10.1107/S0108767391000375

Lyon K, Bergman A, Zeiger P, Kepaptsoglou D, Ramasse QM, Idrobo JC & Rusz J (2021). Theory of magnon diffuse scattering in scanning transmission electron microscopy. *Phys Rev B* **104**, 214418. https://doi.org/10.1103/PhysRevB.104.214418

MacArthur KE, Yankovich AB, Béché A, Luysberg M, Brown HG, Findlay SD, Heggen M & Allen LJ (2021). Optimising experimental conditions for accurate quantitative energy-dispersive X-ray analysis of interfaces at the atomic scale. *Microsc Microanal*. **27**, 528–542. https://doi.org/10.1017/S1431927621000246

Martin AV, Findlay SD & Allen LJ (2009). Model of phonon excitation by fast electrons in a crystal with correlated atomic motion. *Phys Rev B* **80**, 024308. https://doi.org/10.1103/PhysRevB.80.024308

Mendis BG (2019). An inelastic multislice simulation method incorporating plasmon energy losses. *Ultramicroscopy* **206**, 112816. https://doi.org/10.1016/j.ultramic.2019.112816

Mendis BG (2020). Theory underpinning multislice simulations with plasmon energy losses. *Microscopy* **69**, 173–175. https://doi.org/10.1093/jmicro/dfaa003

Mendis BG (2022*a*). Background subtraction in electron Compton spectroscopy. *Micron* **163**, 103363. https://doi.org/10.1016/j.micron.2022.103363

Mendis BG (2022*b*). Quantum theory of magnon excitation by high energy electron beams. *Ultramicroscopy* **206**, 113548. https://doi.org/10.1016/j.ultramic.2022.113548

Mendis BG, Barthel J, Findlay SD & Allen LJ (2020). Inelastic scattering in electron backscatter diffraction and electron channeling contrast imaging. *Microsc Microanal.* **26**, 1147–1157. https://doi.org/10.1017/S1431927620024605

Ophus C (2017). A fast image simulation algorithm for scanning transmission electron microscopy. *Adv Struct Chem Imag.* **3**, 13. https://doi.org/10.1186/s40679-017-0046-1

Ophus C (2019). Four-dimensional scanning transmission electron microscopy (4D-STEM): From scanning nanodiffraction to ptychography and beyond. *Microsc Microanal.* **25**, 563–582. https://doi.org/10.1017/S1431927619000497

Pennycook SJ & Jesson DE (1991). High-resolution Z-contrast imaging of crystals. *Ultramicroscopy* **37**, 14–38. https://doi.org/10.1016/0304-3991(91)90004-P

Peters JJP (2021). A fast frozen phonon algorithm using mixed static potentials. *Ultramicroscopy* **229**, 113364. https://doi.org/10.1016/j.ultramic.2021.113364

Robert HL, Diederichs B & Müller-Caspary K (2022). Contribution of multiple plasmon scattering in low-angle electron diffraction investigated by energy-filtered atomically resolved 4D-STEM. *Appl Phys Lett*. **121**, 213502. https://doi.org/10.1063/5.0129692

Van Dyck D (2009). Is the frozen phonon model adequate to describe inelastic phonon scattering? *Ultramicroscopy* **109**, 677–682. https://doi.org/10.1016/j.ultramic.2009.01.001

Wang ZL (1998). The 'frozen-lattice' approach for incoherent phonon excitation in electron scattering. How accurate is it? *Acta Cryst A* **54**, 460–467. https://doi.org/10.1107/S0108767398001457